Turbulent transport with intermittency: Expectation of a scalar concentration

Mark Peter Rast[*]

Department of Astrophysical and Planetary Sciences, Laboratory for Atmospheric and Space Physics,
University of Colorado, Boulder, Colorado 80309, USA

Jean-François Pinton

Laboratoire de Physique, Ecole Normale Supérieure de Lyon, Université de Lyon, F-69364 Lyon, France

Pablo D. Mininni

Departmento de Fisica, Universidad de Buenos Aires, Buenos Aires, Argentina

Scalar transport by turbulent flows is best described in terms of Lagrangian parcel motions. Here we measure the Eulerian distance travel along Lagrangian trajectories in a simple point vortex flow to determine the probabilistic impulse response function for scalar transport in the absence of molecular diffusion. As expected, the mean squared Eulerian displacement scales ballistically at very short times and diffusively for very long times, with the displacement distribution at any given time approximating that of a random walk. However, significant deviations in the displacement distributions from Rayleigh are found. The probability of long distance transport is reduced over inertial range time scales due to spatial and temporal intermittency. This can be modeled as a series of trapping events with durations uniformly distributed below the Eulerian integral time scale. The probability of long distance transport is, on the other hand, enhanced beyond that of the random walk for both times shorter than the Lagrangian integral time and times longer than the Eulerian integral time. The very short-time enhancement reflects the underlying Lagrangian velocity distribution, while that at very long times results from the spatial and temporal variation of the flow at the largest scales. The probabilistic impulse response function, and with it the expectation value of the scalar concentration at any point in space and time, can be modeled using only the evolution of the lowest spatial wave number modes (the mean and the lowest harmonic) and an eddy based constrained random walk that captures the essential velocity phase relations associated with advection by vortex motions. Preliminary examination of Lagrangian tracers in three-dimensional homogeneous isotropic turbulence suggests that transport in that setting can be similarly modeled.

I. INTRODUCTION

Understanding, predicting, and modeling scalar and vector transport is a key goal of turbulence research. The aim of such efforts is a turbulent transport model that depends only on the statistical properties of the flow, not the detailed dynamics of any single flow realization. If the role of molecular diffusion is small (high Péclet number flows), scalar transport is best described in terms of Lagrangian parcel motions [see early work (e.g. [1–5]), and later reviews (e.g. [6–9]) and the many references therein]. Specific turbulent flow structures, vortices (e.g. [10–12]) or straining stagnation points [13,14], have been identified as likely important to the statistics of those motions, and both of these have been employed as fundamental dynamical components in models of Lagrangian velocity increments [15–17] and pair dispersion [18–21].

In this paper we develop a statistical model of Lagrangian parcel motions as realized in a stochastically driven point vortex flow [17,21]. Our goal is to show that the scalar transport properties of this simplified turbulence analog can be reproduced by a Lagrangian stochastic model based on measurable flow statistics. We compute the probabilistic impulse response function and show that, while to lowest order scalar transport follows random walk statistics, with ballistic

and diffusive scaling at short and long times respectively, higher order departures result from the spatial and temporal intermittency of the flow. Over inertial range time sales, the probability of long-distance transport is reduced below that of a random walk. This is due to vortex trapping delays and can be modeled as a random series of such events. Over very short and very long time scales, on the other hand, long-distance scalar transport is enhanced. At the shortest time scales this is due to individual point vortex contributions, and at the longest it reflects the spatial and temporal variability of the largest scale motions.

The transport equation for a scalar concentrate per unit volume c in an incompressible medium without molecular diffusion can be written in the continuum approximation as

$$\frac{\partial c}{\partial t} + \mathbf{u} \cdot \boldsymbol{\nabla} c = S(\mathbf{x}, t). \tag{1}$$

If the flow field is turbulent, the expectation value of c is given by

$$\langle c(\mathbf{x}, t) \rangle = \int_{-\infty}^{t} \int_{-\infty}^{\infty} P(\mathbf{x}, t | \mathbf{x}', t') S(\mathbf{x}', t') \mathbf{d}\mathbf{x}' dt' \tag{2}$$

(e.g. [8] and references therein), where $S(\mathbf{x}', t')$ is the source distribution and $P(\mathbf{x}, t \,|\, \mathbf{x}', t')$ is the probabilistic impulse response (or Green's) function, the probability density of finding a parcel at $(\mathbf{x}, t)$ given a previous location $(\mathbf{x}', t')$.

---

[*]Corresponding author: mark.rast@lasp.colorado.edu

Similarly, the variance of the concentration can be expressed as

$$\langle c^2(\mathbf{x},t)\rangle = \int P(\mathbf{x},\mathbf{x},t,t|\mathbf{x}_1,\mathbf{x}_2,t_1,t_2)$$
$$\times S(\mathbf{x}_1,\mathbf{x}_2,t_1,t_2)\mathbf{dx}_1\mathbf{dx}_2 dt_1 dt_2 \qquad (3)$$

(e.g. [8] and references therein). Since the flow is turbulent the value of the concentration at any point in space and time $(\mathbf{x},t)$ has a variance that depends on $P(\mathbf{x},\mathbf{x},t,t|\mathbf{x}_1,\mathbf{x}_2,t_1,t_2)$, the probability density that parcels from different locations $(\mathbf{x}_1,t_1)$ and $(\mathbf{x}_2,t_2)$ end up at that position in different flow realizations. This motivates the time reversed pair dispersion problem, though it is more general in time. Note that integrals over all $\mathbf{x}_1$ and $\mathbf{x}_2$ between $\pm\infty$ and all t_1 and t_2 less than or equal to t are implied by the single integral sign in Eq. (3).

If $P(\mathbf{x},t;\mathbf{x}',t')$ and $P(\mathbf{x},\mathbf{x},t,t|\mathbf{x}_1,\mathbf{x}_2,t_1,t_2)$ could be fully specified for a turbulent flow, one could exactly solve for the expectation value of the scalar concentration and its variance at any position and time given a prior source distribution. This is in general not possible; these probability densities must be measured or modeled. The simplest models are Markovian random walk models, with steps δ-correlated in space and time so that the future state of the system depends only on its current state not the sequence of events leading up to it. With Gaussian distributed isotropically directed steps these yield scalar diffusion, with ballistic and diffusive scaling at short and long times respectively [1]. Beyond this, Markovian random flight models incorporate the statistics of the turbulent velocity fluctuations in the solution of a first order stochastic differential equation for the Lagrangian velocity (a Langevin equation) or alternatively a Fokker-Planck equation for the Lagrangian velocity probability density function [22–25]. Such models can account for some temporal correlation along Lagrangian trajectories, and those which take the autocorrelation of the velocity or acceleration to decay exponentially yield solutions with additional time dependence in the diffusion coefficient [15,26]. Departures from diffusive behavior can result from nonfinite variance velocity distributions, nonexponential autocorrelations, or vortex trapping (e.g. [15,27]).

We examine the importance of these processes to scalar transport in a stirred point-vortex flow by measuring the Lagrangian trajectories of passive tracers and constructing the probabilistic impulse response function from them. We find that over inertial range time scales, the probability of long distance transport is reduced from that expected based on a random walk. On shorter and longer time scales, enhanced long-distance transport occurs. Moreover, these behaviors can be successfully modeled using just two flow components, an eddy based random walk and a spatially or temporally intermittent large scale flow, the parameters of which can be determined from measurable properties of the full flow. Preliminary examination of Lagrangian trajectories in fully nonlinear three-dimensional homogeneous isotropic turbulence yields the same behaviors, suggesting that a similar modeling strategy may be useful in that setting.

II. TURBULENT FLOW ANALOG

We employ a simplified stirred point-vortex flow [17] as an analog for highly intermittent turbulence. Point vortices are randomly generated at a constant average rate with Gaussian distributed intensities in a two-dimensional biperiodic domain of dimension $x_{\max}^2$. The velocity field is constructed from the individual contributions of each vortex,

$$\mathbf{u}(\mathbf{x}) = \sum_{k=1}^{N} \frac{\Gamma_k}{2\pi|\mathbf{x}-\mathbf{x}_k|}(\hat{z}\times(\widehat{x-x_k})), \qquad (4)$$

where $\hat{z}$ is perpendicular to the plane of motion, Γ_k are the individual vortices' circulations, and the contribution range of each vortex is truncated at a distance of $|\mathbf{x}-\mathbf{x}_k| = x_{\max}$. Each point vortex moves in the flow generated by all the others with no self-interaction. Vortex merger is imposed when vortices are closer than a fixed critical separation, unit one distance. New vortex positions after merger are taken to be the amplitude-weighted average position of the merged pair, and the new intensities are taken alternatively as either the sum of the circulations or the signed square root of the absolute value of the sum of the signed squared circulations [28]; the first preserves total circulation while the later preserves the total signed squared circulation. This point-vortex system would ultimately decay due to the merger of oppositely signed vortices but for the continuous stirring provided by the generation of new point vortices at random locations in the domain. Thus the algorithm introduces sources and sinks of vorticity and energy not otherwise available to two-dimensional point-vortex systems [17].

We examine the statistics of Lagrangian tracers in these flows, and present the results of three simulations in this paper. Simulation A is an extended version of the simulation presented in [17], but here recomputed with an improved fourth-order Runge-Kutta integration scheme. Simulation B is identical to A except that it employs the energy rather than the circulation conserving merger scheme. Simulation C is identical to B but draws new vortex amplitudes from a distribution that is three times as wide. All other parameters of the simulations are identical. For example, all three simulations are initialized with a same number of vortices randomly placed in the domain (64 in these cases). The total number of vortices increases rapidly before settling down to an equilibrium value which results from a balance between the vortex merger frequency (dynamically determined by the solution) and the vortex creation rate (common to all simulations) [17]. Figure 1 plots solution snapshots for each of these simulations at a late time (at the end of the time series plotted), along with time series of the total vortex number N and interaction energy

$$W = -\frac{1}{4\pi}\sum_{\alpha}^{N}\sum_{\beta}^{N}\Gamma_{\alpha}\Gamma_{\beta}\ln(r_{\alpha\beta}) \qquad (5)$$

in each of them. The double sum in Eq. (5) extends over all vortex pairs ($\alpha \neq \beta$), and $r_{\alpha\beta}$ is the distance between pair members. In an infinite domain of constant point-vortex membership, the interaction energy W is a constant of motion (see e.g. [29]). In our simulations, it shows significant variation with time, due to the model processes of vortex creation and merger and the domain periodicity [17].

The sources and sinks of kinetic energy and enstrophy in these point vortex simulations depend on the merger scheme employed. In the circulation preserving scheme, summing
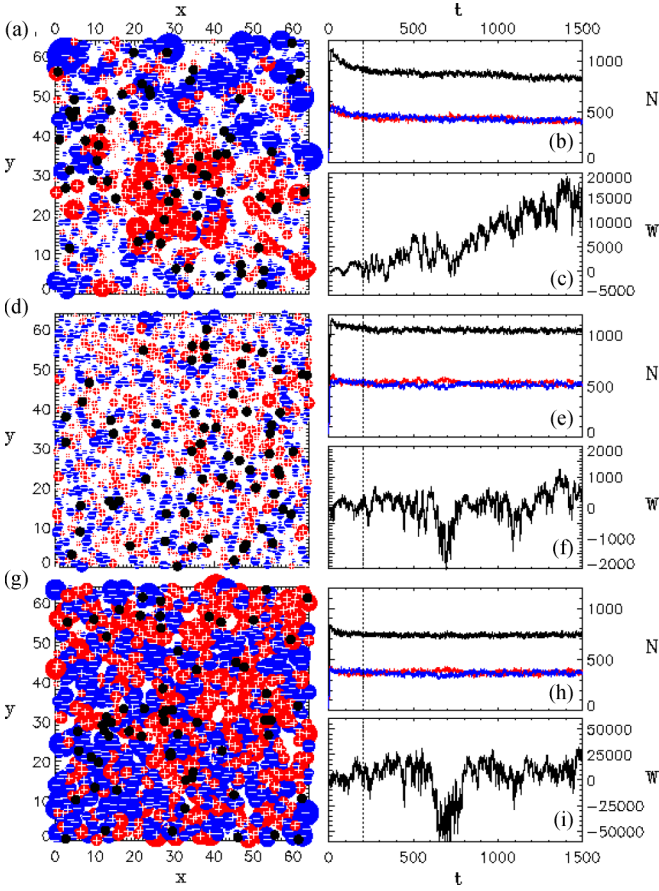
FIG. 1. Snapshots [(a), (d), and (g)], and associated time series [(b) and (c), (e) and (f), and (h) and (i)] to their right, of three point vortex simulations. Simulations A and B [(a) and (d)] sample the same new vortex amplitude distribution and employ circulation conserving and energy conserving merger schemes, respectively. Simulation C [snapshot (g)] draws new vortex amplitudes from a distribution that is three times as wide and employs the same energy conserving merger scheme as B. All three snapshots are taken from the end of the time series plotted and show the instantaneous positions of vortices of positive and negative circulation in *red* and *blue*, respectively, with the magnitude of the symbol indicating the individual point vortex amplitudes. The instantaneous positions of passive Lagrangian tracers are indicated with *black* dots. Time series plots in (b), (e), and (h) show the total vortex number *N* (*black*) and the number of positive (*red*) and negative (*blue*) vortices separately. The interaction energy *W* [Eq. (5)] is plotted as a function of time in panels (c), (f), and (i). Apparent correlations between the time series reflect the simulations' common initial conditions and random number seeds, so that imbalances in the number of positive and negative vortices occur at similar times in the solutions. The circulation conserving merger scheme yields a solution with an inverse energy cascade and a consequent secular increase in *W*, while the energy conserving scheme does not.

like-signed vortices conserves angular momentum but injects kinetic energy because $(\Gamma_1 + \Gamma_2)^2 > \Gamma_1^2 + \Gamma_2^2$, while merging oppositely signed vortices dissipates both angular momentum and energy because in this case $(\Gamma_1 + \Gamma_2)^2 < \Gamma_1^2 + \Gamma_2^2$. In the signed squared circulation preserving scheme, summing like-signed vortices conserves kinetic energy but dissipates angular momentum because $\sqrt{\Gamma_1^2 + \Gamma_2^2} < \Gamma_1 + \Gamma_2$, while summing

oppositely signed vortices dissipates energy and adds angular momentum because $\mathrm{sgn}(\Gamma_1^2 - \Gamma_2^2)\sqrt{|\Gamma_1^2 - \Gamma_2^2|} > \Gamma_1 - |\Gamma_2|$, where Γ_1 is taken to be positive and Γ_2 negative. It is these differences in the merger schemes employed that determine the secular trends in Fig. 1. Simulation A, which employs the circulation conserving merger scheme, shows an inverse energy cascade, the slow accumulation of vortices into two large like-signed groups, and a consequent secular increase in *W*. Simulations B and C, which employ the energy conserving scheme, show large fluctuations in *W* but no secular trends. The apparent correlations between the three time series of *W* in Fig. 1 result because the three runs were started with the same random number seed, yielding imbalances in the total numbers of positive and negative vortices at similar times during the solution.

It is important to note that, while the details (e.g., vortex number density and amplitude distributions) of the statistical flow equilibria achieved in these simulations are affected by the merger scheme and the new vortex amplitude distribution employed, the general scalar transport properties of the flows are not. The transport properties described in this paper are common to all solutions. In fact, they are more generally seen in any two-dimensional collection of point vortices, even one in which neither vortex creation or merger occurs, so long as the vortices dynamically interact [30]. The details of the flow determine the Lagrangian and Eulerian integral time scales, but transport behaviors in relation to these are common to all solutions.

III. PROBABILISTIC IMPULSE RESPONSE

As indicated in Sec. I, if $P(\mathbf{x},t|\mathbf{x}',t')$ could be fully specified for a turbulent flow, the expectation value of the scalar concentration could be calculated exactly for any given source distribution. Such specification is generally not possible, and even direct measurement of $P(\mathbf{x},t|\mathbf{x}',t')$ is overly ambitious as it would require determining the probability that the turbulent flow connects any two space-time points along any possible Lagrangian trajectory.

To make progress, we focus on flows that are isotropic, and take $P(\mathbf{x},t|\mathbf{x}',t') = P(r,t)/2\pi r$, where $r = |\mathbf{x} - \mathbf{x}'|$ and t is redefined as the time interval, $t \equiv \Delta t = t - t'$, with only positive values of t considered to preserve causality. We note that taking $P(r,t)$ to be dependent only on Δt assumes stationarity over the time intervals considered. Small scale motions are indeed statistically stationary in our solutions, but on the largest scales some of the simulations vary slowly with time. Transport on time scales of the largest eddy turnover time or longer is affected by this modulation of the flow amplitudes at the largest scales, and that modulation must be accounted for in any transport model. We undertake this in Sec. IV B below.

We use the motions of the Lagrangian tracers in the point-vortex simulations to measure $P(r,t)$, the distribution of Eulerian distances r traveled via Lagrangian trajectories over time t (the straight line distances particles travel over that time). Starting two hundred time units into each of the simulations (indicated by the vertical *dotted* fiducial lines in Fig. 1), in order to avoid the initial transient solution, we
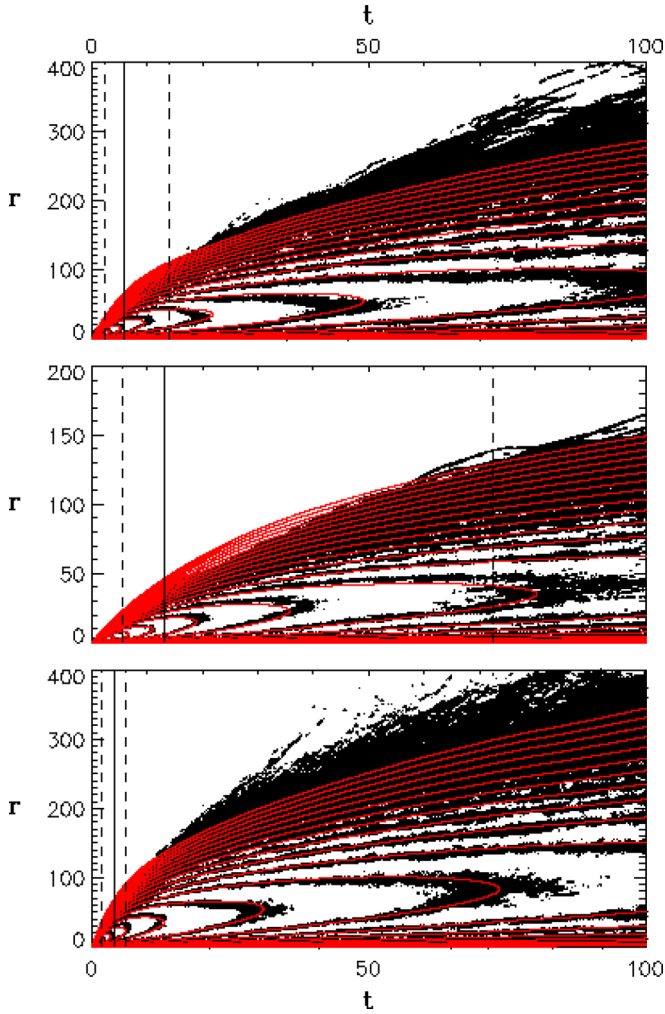
FIG. 2. Contour plots of the logarithm of the probabilistic impulse response, the probability density of traveling an Eulerian distance r in time t along a Lagrangian trajectory, $\log(P(r,t))$. In *black*, contours of $\log(P(r,t))$ measured using the passive Lagrangian tracer trajectories of simulations A (top), B (middle), and C (bottom). In *red*, contours of $\log(P(r,t))$ constructed from the best fit Rayleigh distribution (two-dimensional random walk) to the simulation passive tracer probability density at each time t. Vertical *solid* fiducial lines indicate T_I for each simulation, and vertical *dashed* lines indicate the Lagrangian and Eulerian velocity autocorrelation times at shorter and longer times, respectively.

construct $P(r)$ for a given t (and for multiple values of t) by determining all the Eulerian distances traveled over that time interval anywhere along 64 passive Lagrangian particle trajectories computed during the simulations. We note that, because the vortices themselves have finite lifetimes, we do not employ their trajectories in this calculation. Since the flows are integrated for very long times, any single passive particle trajectory provides many realizations of the Lagrangian path over a given time interval, and thus, despite the relatively low number of particles employed, the distributions obtained are robust even over subsets of the data. Contour plots of $P(r,t)$ are shown in Fig. 2.

The probability density of the Eulerian distance traveled along Lagrangian trajectories $P(r,t)$ approximates that of
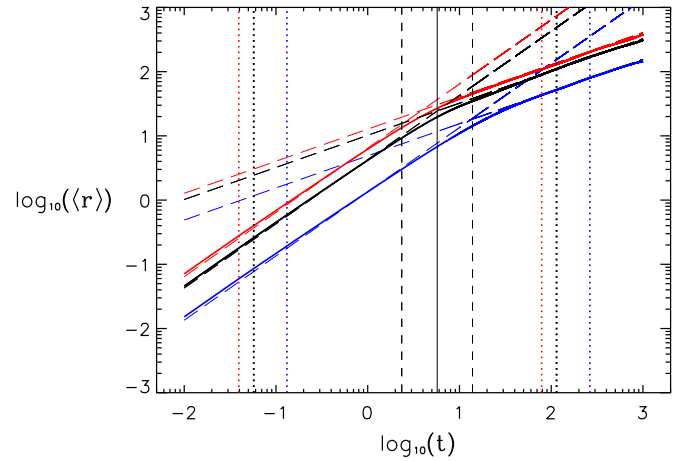

FIG. 3. Expectation value of the Eulerian distance traveled along Lagrangian trajectories $\langle r \rangle$. This scales ballistically at short times (t less than the Lagrangian velocity autocorrelation time) and diffusively for long times (t greater than the Eulerian velocity autocorrelation time). For simulation A (*black* curve), T_I is indicated with a vertical *solid* fiducial line and the velocity autocorrelation times are indicated with vertical *dashed* fiducial lines. For all simulations (simulation B *blue* and simulation C *red*), the ballistic and diffusive scalings are overplotted with *long dashed* lines, and *dotted* vertical fiducial lines indicate $0.01T_I$ and $20T_I$. Cuts through $P(r,t)$ at these times are shown in Fig. 4.

a two-dimensional random walk, a Rayleigh distribution, $P(r,t) = r/\sigma^2 \exp(-r^2/2\sigma^2)$ (Fig. 2, *red* curves), with the variance σ^2 proportional to $\langle r^2 \rangle$ and a function of the time interval t. The variance scales ballistically, as t^2, for short time intervals and diffusively, as t, for long time intervals. This is true of all the point vortex simulations examined (Fig. 3). The crossover time between ballistic and diffusive behavior, hereafter labeled T_I, is indicated with vertical *solid* fiducial lines for all simulations in Fig. 2 and for simulation A in Fig. 3. If transport by a turbulent flow could be reduced to a random walk, then it would be well described as diffusion, and only $\sigma(t)$ would be needed to compute the expectation of the scalar concentration. This is not the case.

The true probabilistic impulse response function $P(r,t)$ required to compute $\langle c(\mathbf{x},t) \rangle$ shows significant departures from the Rayleigh random-walk distribution (Figs. 2 and 4). Over time intervals either short compared to the Lagrangian velocity autocorrelation time or long compared with the Eulerian velocity autocorrelation time (these shown with vertical *dashed* fiducial lines for all three simulations in Fig. 2 and for simulation A in Fig. 3), the probability of long distance transport is enhanced over that of a random walk. Over intermediate time intervals (inertial range time scales), however, the probability of long distance transport is substantially reduced compared to that of a random walk. Figure 4 shows plots of $P(r,t)$ from the simulations at fixed times: $t = 0.01T_I$ (for simulation A this is about 0.025 times the Lagrangian autocorrelation time), $t = T_I$, and $t = 20T_I$ (for simulation A the later is about 8.25 times the Eulerian autocorrelation time). For reference, the shortest time interval for which the distributions are shown [$t = 0.01T_I$ in Fig. 4(a)] is 6, 13, and 4 simulation time steps long in Simulation A,
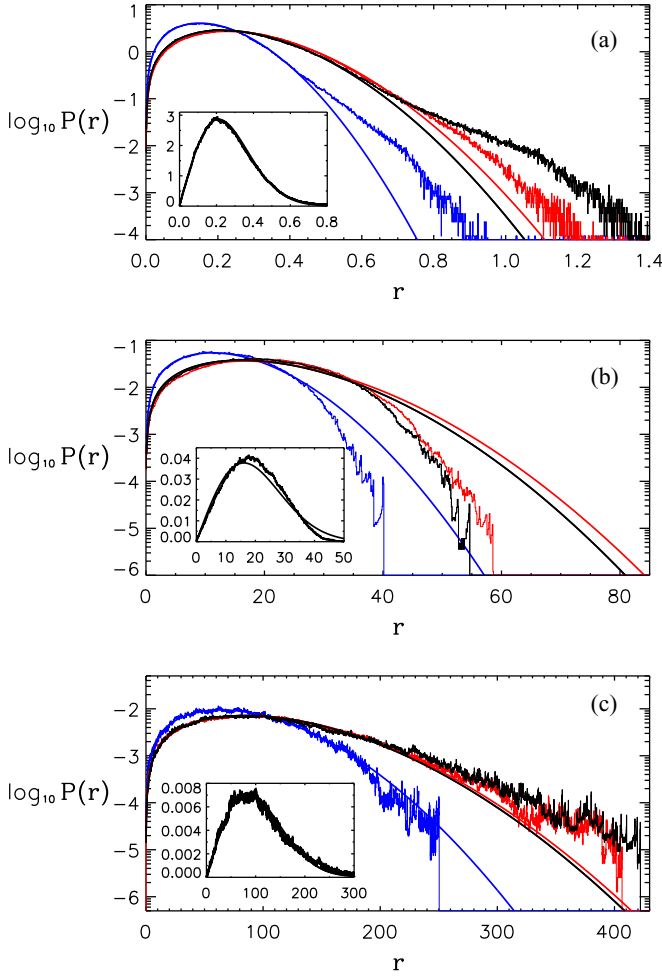
FIG. 4. Probabilistic impulse response function $P(r,t)$ at fixed times (a) $t = 0.01T_I$, (b) $t = T_I$, and (c) $t = 20T_I$ measured using the passive Lagrangian tracer trajectories of simulations A (*black*), B (*blue*), and C (*red*). These are vertical cuts through the two-dimensional probability density functions contoured in Fig. 2. The probability of long distance transport is enhanced over the best fit two-dimensional random walk Rayleigh distribution (overplotted with *solid* curves) at very short and, in some cases, very long times [(a) and (c)] but suppressed over intermediate (inertial range) time scales (b). Inset plots show the cores of the simulation A distributions in more detail, illustrating the distortion of the core from Rayleigh at intermediate times.

B, and C, respectively. This is very much shorter than the Lagrangian autocorrelation time in any case. The best fit Rayleigh distributions are also shown in Fig. 4. Those random walk distributions approximate the cores of the measured probability density functions but not their tails, though it is important to note that over inertial range times scales even the cores of the distributions are distorted [see Fig. 4(b) inset]. The probability of long distance transport (the distribution tail) is enhanced at very short times and, in some cases, very long times [Figs. 4(a) and 4(c)] but suppressed over intermediate (inertial range) time scales [Fig. 4(b)]. The very long time enhancement of long distance transport is particularly surprising as it occurs for times long compared to any correlation time in the flow.
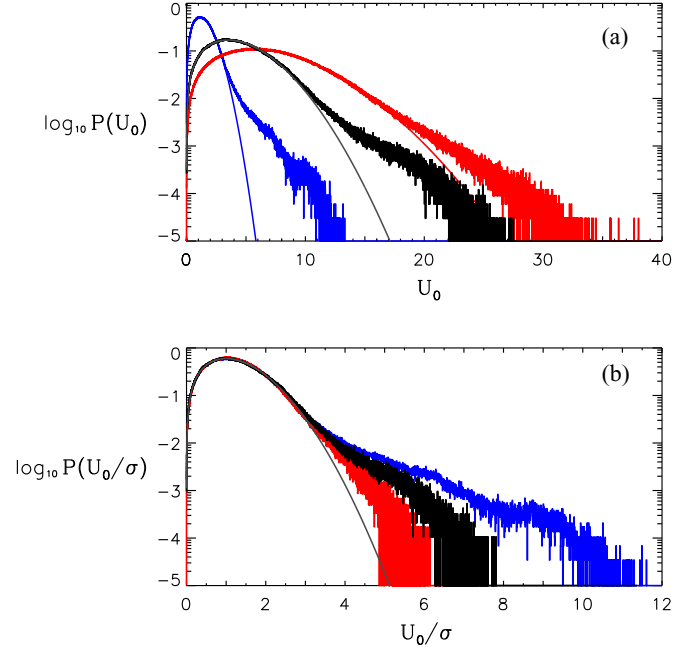

FIG. 5. Distributions of the Lagrangian particle speed U_0 in the three simulations, A (*black*), B (*blue*), and C (*red*), with Rayleigh distribution fits overplotted with *solid* curves of the same color. In (b) the Lagangian speed has been scaled by the width of the best fit Rayleigh distribution σ.

These deviations in transport probability densities, from those of a random walk, can be qualitatively understood as follows. At very short times [Fig. 4(a)], the Lagrangian distance traveled reflects the underlying distribution of step sizes. The particle motions are dominated by single vortex interactions and configurations, as the time interval is too short (well below the Lagrangian integral time) for multiple sequential vortex interactions or the evolution of the vortex configuration to be important. The distribution of distances traveled over very short time intervals thus reflects ballistic motion with speeds sampled from the underlying Lagrangian speed distribution. The Lagrangian speed distribution is not necessarily Rayleigh, and often has a high speed tail (Fig. 5). This may be due to the singular nature of the point vortex flow we are examining, but the exact shape of the distribution also depends on the simulation details. Somewhat counterintuitively, solutions with high numbers of low amplitude vortices (such as simulation B) show more pronounced high speed tails [Fig. 5(b)]. This likely reflects the dominance of nearest neighbor vortex contributions in those flows [17].

The short time impulse response functions of all the simulations can to some extent be captured by artificial displacement time series explicitly constructed using velocity components with the same auto and cross correlations as those observed in the simulation data. To do this [31], the Fourier transform of the artificial x velocity time series $\tilde{u}_x$ is determined from the Fourier transform of the autocorrelation of the point-vortex simulation Lagrangian velocity time series $\tilde{A}$ as

$$\tilde{u}_x = \sqrt{\tilde{A}}\, e^{i\delta_x}, \qquad (6)$$

taking the modes to have uniformly distributed random phases, $0 \geqslant \delta_x < 2\pi$. The Fourier transform of the artificial y velocity time series $\widetilde{u}_y$ is constructed from that of $\widetilde{u}_x$ as

$$\widetilde{u}_y = \widetilde{u}_x e^{-i\delta_y}, \qquad (7)$$

with the phases δ_y taken to be

$$\delta_y = -i \ln\left(\frac{\widetilde{C}}{\widetilde{A}}\right), \qquad (8)$$

where $\widetilde{C}$ is the Fourier transform of the cross correlation of the point-vortex simulation Lagrangian velocity component time series. By the Wiener-Khinchin and cross-correlation theorems the final artificial velocity time series thus constructed share the point vortex simulation Lagrangian velocity auto and cross correlations. Importantly, however, unlike for the real Lagrangian trajectories, the phases of the Fourier components that make up the velocity time series in this construction are random.

Over very short time intervals the long distance tail of the probability density of the Eulerian distance traveled along trajectories determined using these artificial velocity time series is elevated over that of a random walk, as in the point vortex simulation [Fig. 6(a)]. This is because, for these very short times, few steps have been taken, the motions are strictly ballistic at each time step with the distance traveled given by the speed and elapsed time, and the underlying speed distribution is non-Rayleigh (Fig. 5). The tail of the artificial time series distribution falls somewhat short of that of the Lagrangian motions in the point vortex simulation (over the range of distance values shown in the plot) because the phase continuity of the eddy motions in the simulation is not captured by the random phase prescription used in the construction of the artificial velocity components. For longer distances than those show in the plot the tail of the artificial time series distribution should exceed that of the simulations because of the finite eddy size limit in the real flow (see trapping discussion below).

The importance of the nonrandom phase to Lagrangian motions in the point vortex simulation is even more apparent at longer time intervals; displacement time series constructed to share the observed velocity component auto and cross correlations do not yield the observed $P(r,t)$ distributions at intermediate and long time intervals, producing instead Rayleigh or nearly Rayleigh random walk distributions [Figs. 6(b) and 6(c)]. At intermediate (inertial range) times the phase relations between the velocity components are particularly critical to the real flow. Random vector orientations can capture the observed auto and cross correlation of the velocity components, as they were explicitly constructed to do in the artificial time series, without reproducing the dynamical trapping events which result from coherent eddy motions in the point vortex simulations. Similarly, long-distance transport over long time intervals depends on key flow dynamics, in this case the time variability of the large scale flow, again only captured in part by the auto and cross correlations.

Unlike for short and intermediate times, for which all point vortex simulations show deviations of $P(r,t)$ from Rayleigh, only some of the simulations show the prominent long-time long-distance excess [Fig. 4(c)]. Moreover, the long-time
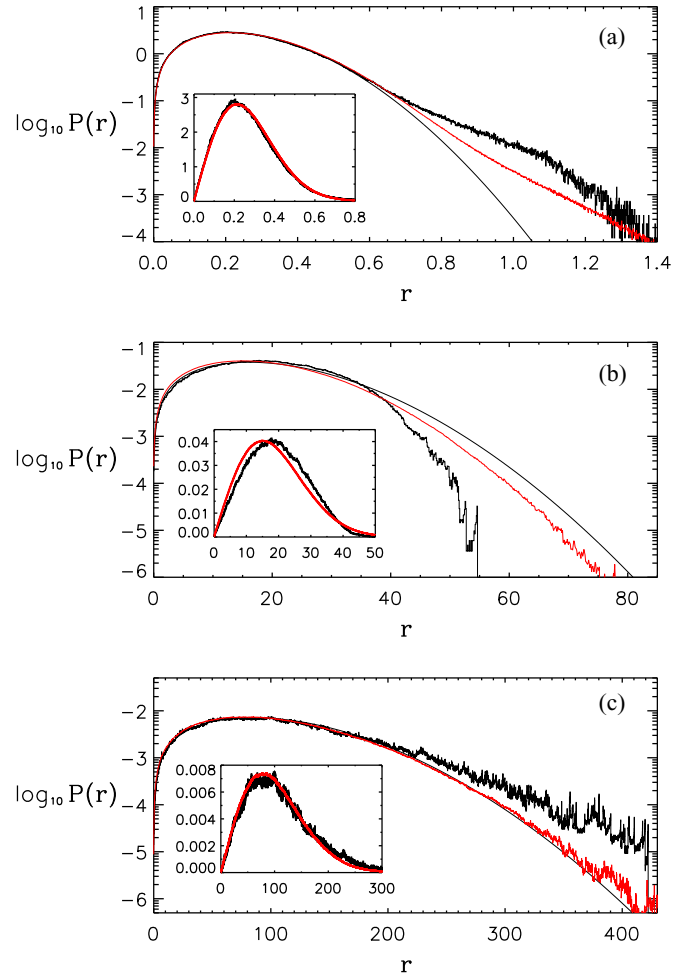

FIG. 6. Probabilistic impulse response function $P(r,t)$ at fixed times (a) $t = 0.01T_I$, (b) $t = T_I$, and (c) $t = 20T_I$ for Lagrangian trajectories extracted from the point vortex flow (*black* curves) and trajectories calculated from velocity component time series constructed to share the same auto and cross correlations as those observed in the point vortex simulations (*red* curves). For clarity only the results for simulation A are plotted.

excess does not depend directly on the vortex merger scheme employed; it is found in simulations both with and without an inverse cascade. We find instead that the enhanced distribution tail at long times requires the presence of a spatially and/or temporally intermittent large scale flow. A constant and uniform large scale flow adds only a Galilean invariant mean to the particle trajectories, with the net effect on the Eulerian distances traveled depending only on the trajectory directions. The variance of the resulting distribution increases but the distribution shape is unaltered, remaining Rayleigh at long times as in simulation B [Fig. 4(c), *blue*]. In that simulation the distribution approaches the Rayleigh distribution from below as the time interval increases because vortex trapping, which dominates at intermediate times, becomes increasingly less likely for times longer than the Eulerian integral time and the Lagrangian trajectories become increasingly autodecorrelated. If the large scale flow is spatially or temporally intermittent, however, Lagrangian particles each sample the large scale flow for different amounts of time along their trajectory

thus effectively sampling underlying Rayleigh distributions of different widths. Summed together these yield the distribution with the characteristically elevated tail seen in some of our simulations at long times [simulations A and C, Fig. 4(c), *black* and *red*]. Equivalently the enhanced long-time long-distance tail can be artificially reproduced by a series of random walks which differ in the total number of steps taken. We explicitly illustrate the dependence of the long-time enhancement on the large scale flow variability realized in simulation A in Sec. IV C below.

The deviations of $P(r,t)$ from the two-dimensional random walk distribution described above can be captured using a highly simplified scalar transport model, one that relies on measurable properties of the flow, not flow simulation, to duplicate the probabilistic Green's function of the real flow. In order to construct such a model the key dynamics discussed above must be accounted for.

IV. STATISTICAL TRANSPORT MODEL

The goal is to model the scalar transport probabilistic impulse response function $P(r,t)$ using only measurable statistics of the flow, so that the expectation of the scalar concentration can be calculated for any source distribution without explicit computation of the flow itself. The challenge is that two-dimensional random walk processes with finite variance step size distributions (as the Lagrangian velocity distribution in our point-vortex simulation) robustly yield Rayleigh distributions for $P(r,t)$. Correlations between velocity components, not random phases, are thus required, but even then purely circular motions (the underlying dynamics of a point vortex flow) are indistinguishable from random vector orientations if eddy trapping is not accounted for.

We find that a simplified yet accurate model of scalar transport in a point vortex flow can be constructed using just two components: an eddy constrained random walk and a spatially or temporally intermittent large scale flow. The first of these is determined by the statistical properties of the flow, while the second requires explicit knowledge of the amplitudes of its lowest wave number components, ($[k_x,k_y] = [0,0]$, $[0,1]$, $[1,0]$, and $[1,1]$). With these ingredients $P(r,t)$ can be reconstructed.

A. Eddy constrained random walk

To statistically capture in a random walk formulation the underlying velocity component phase relationships and temporal continuities, we take the flow geometry to be circular motion and thus the Eulerian distance dr traveled after each step as the chord of a circle traveled by the Lagrangian parcel

$$dr = 2r_t|\sin\theta|, \qquad (9)$$

where r_t is the radius of the circular trapped motion and θ is the central angle given by

$$\theta = \frac{U_0}{r_t}t_t. \qquad (10)$$

Here U_0 is the magnitude of the Lagrangian velocity, and the circular motion is taken to persist for a time t_t. We note that a random walk constructed from such steps is Markovian, in

the sense that each step is independent of the previous as the particle moves from one eddy to the next, but importantly, memory is introduced into the random walk at the eddy scale. Since the motions are circular, the acceleration of the fluid parcel is autocorrelated within each trapping eddy, though memory is lost between steps.

Given distributions of eddy size $P(r_t)$, trapping time $P(t_t)$, and Lagrangian particle velocity $P(U_0)$, we construct random walk trajectories from the motions induced by successive uncorrelated eddies each entered with a random phase. Equivalently the random walk is constructed as a sum over steps of length dr determined from Eqs. (9) and (10) taken in random directions after time t_t. The result is a continuous-time random walk (e.g. [32–34]), but one in which the step size and time delays are nonlinearly related [Eqs. (9) and (10)] and determined from distributions of physically motivated variables: eddy size, circulation speed, and trapping time. Remarkably, the trap radius r_t (eddy size), Lagrangian velocity U_0 (circulation speed), and trapping time t_t that determine dr can be chosen *independently* from simple physically motivated distributions, and when the resulting constrained random walk is combined with advection by the lowest wave number components of the flow, the trajectories yield the correct probabilistic Green's function $P(r,t)$.

Motivated by previous work [21], we take the trapping time distribution $P(t_t)$ to be uniform between zero and the Eulerian integral time. The Eulerian integral time is measured by an exponential fit to the autocorrelation of one component of the velocity at fixed position in the point vortex simulation. This sets that the longest possible time a Lagrangian particle can remain trapped in an eddy to be equal to the characteristic eddy lifetime. Further, we take $P(U_0)$ to be that observed in the point-vortex simulation or, if $P(r,t)$ is not needed at very short times, the speed distribution can be approximated by a Rayleigh fit to its core (Fig. 5) and only the width of the distribution is needed. Finally, the eddy trap size is taken to be distributed as length in Kolmogorov turbulence $P(r_t) \sim r_t^{4/3}$ for $r_t \leqslant L/2 = x_{\max}/4$, where L is Eulerian integral length; larger higher-energy eddies are the dominant trapping structures. One-half the integral length is chosen for the largest eddy in the eddy constrained random walk because a Lagrangian particle cannot escape the largest eddy in the domain. Eddies of size $L = x_{\max}/2$, the lowest wave number harmonic mode of the domain, are treated along with any mean flow as large scale motions upon which the random walk is superimposed. We note that imposing a small eddy cutoff (at the Kolmogorov scale) had no noticeable impact on the solutions and was omitted for simplicity.

B. Low wave number contributions

In addition to the eddy constrained random walk described above, the statistical transport model accounts for domain scale motions. These are modeled as contributions that depend on the Eulerian position of the Lagrangian parcel; the eddy constrained random walk is superimposed on the largest scale motions in the domain, with the local parcel velocity equal to the sum of the random walk velocity and the lowest spatial wave number component of the turbulent flow at the parcel's Eulerian position.
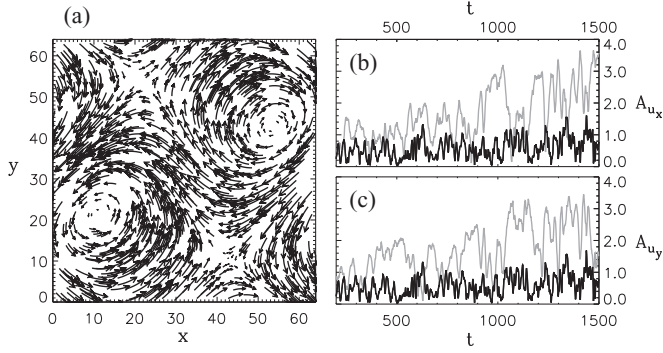
FIG. 7. Vector plot of the flow reconstructed from the time average amplitudes of the smallest wave number harmonic modes (a), with arrow positions chosen randomly and arrow lengths indicating relative flow speeds. The magnitudes of the complex amplitudes of the lowest nonzero wave number modes, in (b) u_x $[k_x,k_y] = [0,1]$ (*gray*) and $[1,1]$ (*black*) and in (c) u_y $[k_x,k_y] = [1,0]$ (*gray*) and $[1,1]$ (*black*), are plotted as a function of time t.

While typically this large scale flow would be readily observed or extracted from a numerical solution, determining it in our case requires significant computational effort. The n-body point vortex contributions must be reconstructed on a grid, Fourier transformed, and filtered. With many hundreds of individual vortices contributing to the velocity at every point in the domain (Fig. 1) and hundreds of thousands of time steps computed over the course of each simulation, this reconstruction of the discretized velocity field from the n-body point-vortex solution is quite expensive. We present here the results for simulation A only, as reconstructed on a 512^2 grid evaluated every 10 time steps (with the step size in the simulation equal to 0.01 time units on the plots). The same calculations were done for simulation C, which does not show an inverse cascade, and support the conclusions we present.

The finite resolution of the low wave number reconstruction, compared to that of the n-body point vortex flow itself, means that in modeling $P(r,t)$ (Sec. IV C below) the large scale flow is well resolved over long times and large scales but less so over short times and lengths. The full effects of this on the statistical transport model are not completely understood and may contribute to the difficulty the model has in obtaining the correct distribution core widths at short and intermediate time scales. Inadequate resolution of the large-scale flow over short time scales leads to an overestimation of the distance traveled over those times since flow variations not captured could facilitate cancellation by directional changes. The magnitude of this effect may however be too small to explain model difficulties below.

The large scale flow in simulation A evolves significantly with time. Figure 7 illustrates the structure and variability of the largest scale flows in the domain. Shown are the magnitudes of the complex amplitudes of the u_x velocity $[k_x,k_y] = [0,1]$ and $[1,1]$ modes and the u_y velocity $[k_x,k_y] = [1,0]$, and $[1,1]$ modes as a function of time, along with a vector plot of the flow reconstructed from the the time average amplitudes of those modes. The remaining largest scale modes ($[k_x,k_y] = [0,0]$, and $[1,0]$ for u_x and $[k_x,k_y] = [0,0]$, and $[0,1]$ for u_y) have lower amplitudes by an order of magnitude or more. The
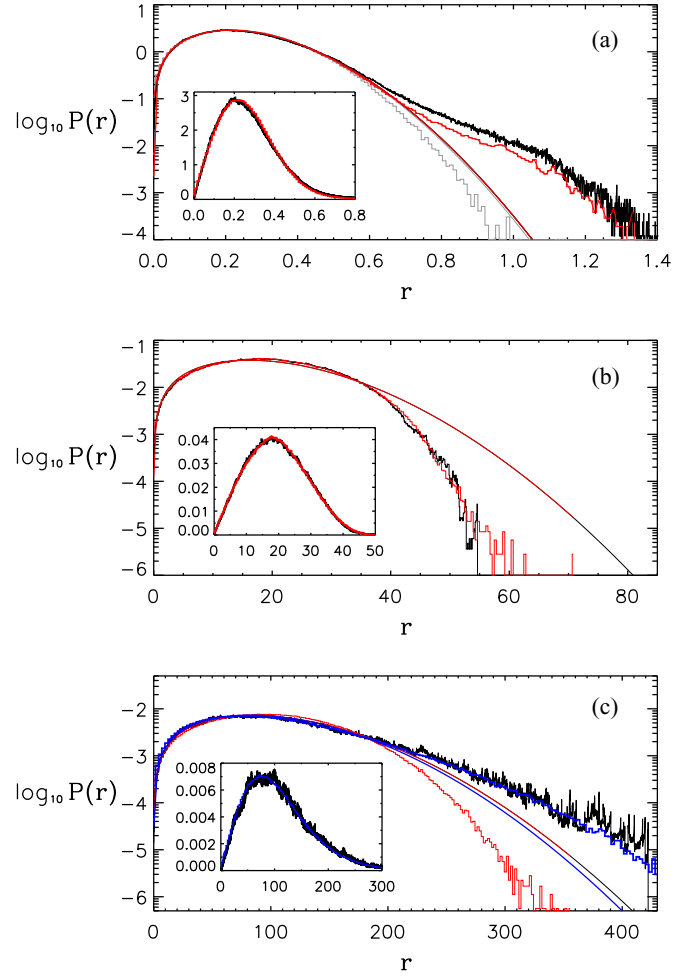

FIG. 8. Two component model of scalar transport. The *black* curves are cuts through the probabilistic impulse response function $P(r,t)$ of simulation A at fixed times $t = 0.01T_I$, T_I, and $20T_I$ (as in Fig. 4). The *red* curves plot the probability densities of the Eulerian distance traveled by the constrained random walk superimposed with random orientation on the temporal average large scale flow in the simulation [Fig. 7(a)]. These have been scaled by the point-vortex flow Rayleigh distribution fit widths (*solid* curves). The *gray* curve in panel (a) plots the short time distribution if only the Rayleigh fit to the Lagrangian velocity core is used in the constrained random walk. The *blue* curve in panel (c) shows the model results when the actual temporally evolving large-scale component of the point vortex flow (rather than its temporal average) is employed in the model.

inverse energy cascade, and the consequent secular increase in the large scale flow amplitude discussed earlier (Sec. II), is clearly apparent in the amplitudes of the u_x $[k_x,k_y] = [0,1]$ and the u_y $[k_x,k_y] = [1,0]$ modes. Perhaps more importantly for modeling the transport probabilities, the amplitudes of the large scale modes show temporal variability down to the resolution of the Eulerian velocity reconstruction. The large-scale eddies evolve in amplitude and form even over quite short time intervals.

C. Model results

Figure 8 illustrates how these simple components combine to reproduce the probabilisitic Green's function $P(r,t)$ of the full point-vortex turbulent flow analog. The *black* curves are cuts through the probabilistic impulse response function of simulation A at fixed times $t = 0.01T_I$, T_I, and $20T_I$ (as in Fig. 4). The *red* curves plot the probability densities of the constrained random walk distances from the origin after the same elapsed times. One million constrained random walk trajectories were constructed as described above, superimposed with random orientations on the average large scale flow of Fig. 7(a). Since the average flow is taken to be steady, its influence may be overestimated (as discussed in Sec. IV B), and the distribution widths have been scaled by factors of about 0.95, 0.88, and 0.74 for $t = 0.01T_I$, T_I, and $20T_I$, respectively. These scalings are the ratio of the full point-vortex and two-component model Rayleigh distribution fit widths.

The scaled steady model distribution shapes fit the data at short and intermediate times very well. As discussed previously (Sec. III), the non-Rayleigh tail of the short time distribution [Fig. 8(a)] results directly from the tail of the Lagrangian speed distribution (Fig. 5). If only the Rayleigh fit to the low speed core is employed in the constrained random walk component of the model, the enhanced short-time long-distance travel tail disappears. This is illustrated in Fig. 8(a) in *gray*. We note that whether the full Lagrangian speed distribution or the Rayleigh fit to it is used has very little effect on the probability densities at later times, and model results using the full distribution are plotted in Figs. 8(b) and 8(c).

At intermediate time intervals, those for which trapping is important, the probabilistic Green's function of the point vortex flow is well captured by the simplified model. We note in particular that the flattened shape of the distribution core is reproduced [Fig. 8(b) inset] along with the tail deficit. This core shape is quite difficult to obtain, and results here only by the combination of the two components; both the constrained random walk and the large-scale Eulerian flow are required. This is likely why the intermediate time distribution of simulation B, the simulation for which there is little evidence of the influence of a large-scale flow at long times, shows little distortion in its core [Fig. 4(b), *blue* curve].

Over time intervals long compared to the Eulerian integral time, the steady mean large-scale flow does not capture the real flow behavior, and the model pdf does not match the probabilistic impulse response of the point vortex data [Fig. 8(c), *red*]. As discussed previously the elevated tail at these late times reflects the nonsteady nature of the large-scale flow. We illustrate this by utilizing the reconstructed flow time series directly. Starting each constrained random walk at a uniformly random location and time, we advect the particle based on the evolving amplitude of the low wave number modes (the mean and lowest harmonic) at its Eulerian position in the point vortex solution. Despite the somewhat low temporal resolution of the flow evolution (necessitated by the expense of the Eulerian flow reconstruction), when the large scale flow is accounted for in this way $P(r,t)$ is reproduced. This is illustrated by the *blue* curves in Fig. 8(c). The long-time

large-distance excess can be reproduced by introducing the observed time variability of the large scale flow.

The same was not true for the short and intermediate time transport pdfs. At those shorter times the reconstructed low wave number flow, when combined with the constrained random walk in the transport model, had too large an amplitude to reproduce the probabilistic impulse response. It is unclear why this is the case or why at these shorter times using the time averaged large scale flow in the model reproduces the distribution shapes extremely well but not their widths without scaling. These issues may be related to the mixed Eulerian-Lagrangian formulation of the two component model; the largest eddy in the domain is not exactly equivalent to the lowest wavenumber Eulerian component as we have assumed in the model. Resolution of these difficulties remains the focus of current research, but it is notable that the model could potentially inform a true parameterless large-eddy subgrid model of scalar transport. It requires only the observed amplitude evolution of the lowest wave number modes (the mean and the lowest harmonic) and measurable statistics of the smaller scale flows (used in a constrained eddy to eddy random walk) to reproduce the scalar transport probabilistic impulse response function. With this in hand, and for any given initial source distribution, the expectation value of a scalar concentration at any location in space and time could then be predicted.

V. CONCLUSION

We have demonstrated for a turbulent analog flow that, while the expectation value of the Eulerian distance traveled scales ballistically at short times and diffusively at long, the full probability density of the Eulerian distance traveled along Lagrangian trajectories deviates from that of a random walk and therefore scalar transport cannot be treated as a diffusion process. We have interpreted the observed deviations from random walk behavior in terms of small-scale flow intermittency and large-scale flow variability, and modeled the effects using two flow components: measured amplitudes of the lowest wave number modes and a constrained random walk based on successive vortex trapping. The later depends only on independently sampled distributions that describe successive independent trapping events: a Kolmogorov eddy size distribution, uniformly distributed trapping times, and a Lagrangian speed distribution that for all but the shortest time intervals can be taken as Maxwellian (Rayleigh in two dimensions).

Preliminary work shows that significant deviations from random walk distributions also occur for the Eulerian distance traveled by Lagrangian particles in fully nonlinear simulations of three-dimensional homogeneous isotropic turbulence. In such simulations the Lagrangian speed distribution is nearly Maxwellian so no deviation occurs at the shortest time intervals, but at intermediate times a similar deficit in long distance travel to that observed in the point-vortex flow is found. The deficit differs somewhat in form because account must be taken of motions parallel to the underlying randomly oriented vortex filaments in addition to the trapping motions in the planes perpendicular to them. As in the point vortex flow, at long times (longer than the Eulerian integral time) the three-dimensional turbulence simulations show a long-distance

excess that depends on the presence of an unsteady large-scale flow component. These similarities suggest that the scalar transport probabilistic impulse response function $P(r,t)$ for three-dimensional homogeneous isotropic and incompressible turbulence can be modeled in a way similar to that presented here, and that the expectation value of a scalar concentration in such turbulence can be predicted, given a source distribution, based exclusively on the amplitude of the lowest wave number modes and readily measurable statistics of the flow.

The success achieved in quantitatively reproducing the transport behavior of the turbulence analog flow is noteworthy. The eddy based constrained random walk description captures fundamental turbulent intermittency effects that reduce long-distance transport over inertial range time scales. It does so by incorporating essential velocity phase relationships into the statistical description of the step sizes and durations, thereby capturing the dynamics of vortex trapping. The enhancement of long-distance transport at long times is also captured, in this case by including the nonstationarity of the flow at the largest scales. These distribution tails play an important role in risk assessment, and the model potentially provides a way to compute scalar transport probabilities that could be used instead of solving directly for particle motions. The fluid equations must still be solved (or the flow observed), but only to obtain the statistics of the flow, the eddy size, trapping time, and Lagrangian velocity distributions, and possibly the largest scale flow amplitudes if they are time varying. Once these are obtained, the expectation of the scaler concentration at any location and time can be computed from the modeled transport probability distribution function given any source distribution. Similar modeling of the concentration variance requires that the generalized and time reversed pair dispersion probability density $P(\mathbf{x},\mathbf{x},t,t|\mathbf{x}_1,\mathbf{x}_2,t_1,t_2)$ can similarly be reconstructed base on the presumed underlying eddy dynamic.

[1] G. I. Taylor, Proc. London Math. Soc. **S2-20**, 196 (1922).

[2] L. F. Richardson, Proc. R. Soc. London Ser. A **110**, 709 (1926).

[3] L. F. Richardson, Beitr. Phys. Frei. Atmos. **15**, 24 (1929).

[4] G. K. Batchelor, Aust. J. Sci. Res. **2**, 437 (1949).

[5] G. K. Batchelor, Proc. Cambridge Philos. Soc. **48**, 345 (1952).

[6] J. D. Wilson and B. L. Sawford, Boundary-Layer Meteorol. **78**, 191 (1996).

[7] H. Rodean, Meteor. Monographs **26**, 1 (1996).

[8] B. Sawford, Annu. Rev. Fluid Mech. **33**, 289 (2001).

[9] F. Toschi and E. Bodenschatz, Annu. Rev. Fluid Mech. **41**, 375 (2009).

[10] A. LaPorta, G. A. Voth, A. M. Crawford, J. Alexander, E. Bodenschatz, Nature (London) **409**, 1017 (2001).

[11] L. Biferale, G. Boffettta, A. Celani, A. Lanotte, and F. Toshi, Phys. Fluids **17**, 021701 (2005).

[12] N. Mordant, P. Metz, O. Michel, and J.-F. Pinton, Phys. Rev. Lett. **87**, 214501 (2001).

[13] J. C. H. Fung, J. C. R. Hunt, N. A. Malik, and R. J. Perkins, J. Fluid Mech. **236**, 281 (1992).

[14] J. C. H. Fung and J. C. Vassilicos, Phys. Rev. E **57**, 1677 (1998).

[15] C. Pasquero, A. Provenzale, and A. Babiano, J. Fluid Mech. **439**, 279 (2001).

[16] M. Wilczek, F. Jenko, and R. Friedrich, Phys. Rev. E **77**, 056301 (2008).

[17] M. P. Rast and J.-F. Pinton, Phys. Rev. E **79**, 046314 (2009).

[18] J. Dávila and J. C. Vassilicos, Phys. Rev. Lett. **91**, 144501 (2003).

[19] S. Goto and J. C. Vassilicos, New J. Phys. **6**, 65 (2004).

[20] T. Faber and J. C. Vassilicos, Phys. Fluids **21**, 015106 (2009).

[21] M. P. Rast and J.-F. Pinton, Phys. Rev. Lett. **107**, 214501 (2011).

[22] P. A. Durbin, NASA Ref. Pub. No.1103, 1983 (unpublished).

[23] B. L. Sawford, Q. J. R. Met. Soc. **109**, 339 (1983).

[24] D. J. Thomson, Q. J. R. Met. Soc. **110**, 1107 (1984).

[25] D. J. Thomson, J. Fluid Mech. **180**, 529 (1987).

[26] B. L. Sawford, Phys. Fluids A **3**, 1577 (1991).

[27] A. Provenzale, A. Babiano, A. Bracco, C. Pasquero, and J. B. Weiss, Lect. Notes Phys. **744**, 101 (2008).

[28] Thanks to J. Weiss for this suggestion.

[29] D. M. F. Chapman, J. Math. Phys. **19**, 1988 (1978).

[30] Lagrangian motions in a collection of vortices with fixed nonevolving positions do not show the same statistical properties as those in an advectively interacting collection of vortices with constantly changing positions because Lagrangian trajectories in the static configuration are periodic.

[31] Thanks to B. Hindman for suggesting this method.

[32] B. D. Hughes, *Random Walks and Random Environments, Vol. 1 Random Walks* (Clarendon Press, New York, 1995).

[33] P. de Anna, T. Le Borgne, M. Dentz, A. M. Tartakovsky, D. Bolster, and P. Davy, Phys. Rev. Lett. **110**, 184502 (2013).

[34] S. Thalabard, G. Krstulovic, and J. Bec, J. Fluid Mech. **755**, R4 (2014).